

The role of viscosity on drop impact forces

Vatsal Sanjay^{1†}, Bin Zhang^{2‡}, Cunjing Lv^{2¶}, and Detlef Lohse^{1,3||}

¹Physics of Fluids Group, Max Planck Center for Complex Fluid Dynamics, Department of Science and Technology, and J. M. Burgers Centre for Fluid Dynamics, University of Twente, P. O. Box 217, 7500 AE Enschede, The Netherlands

²Department of Engineering Mechanics, AML, Tsinghua University, Beijing 100084, China

³Max Planck Institute for Dynamics and Self-Organization, Am Fassberg 17, 37077 Göttingen, Germany

(Received xx; revised xx; accepted xx)

A liquid drop impacting a rigid substrate undergoes deformation and spreading due to normal reaction forces, which are counteracted by surface tension. On a non-wetting substrate, the drop subsequently retracts and takes off. Our recent work (Zhang et al., *Phys. Rev. Lett.*, vol. 129, 2022, 104501) revealed two peaks in the temporal evolution of the normal force $F(t)$ – one at impact and another at jump-off. The second peak coincides with a Worthington jet formation, which vanishes at high viscosities due to increased viscous dissipation affecting flow focusing. In this article, using experiments, direct numerical simulations, and scaling arguments, we characterize both the peak amplitude F_1 at impact and the one at take off (F_2) and elucidate their dependency on the control parameters: the Weber number We (dimensionless impact kinetic energy) and the Ohnesorge number Oh (dimensionless viscosity). The first peak amplitude F_1 and the time t_1 to reach it depend on inertial timescales for low viscosity liquids, remaining nearly constant for viscosities up to 100 times that of water. For high viscosity liquids, we balance the rate of change in kinetic energy with viscous dissipation to obtain new scaling laws: $F_1/F_\rho \sim \sqrt{Oh}$ and $t_1/\tau_\rho \sim 1/\sqrt{Oh}$, where F_ρ and τ_ρ are the inertial force and time scales, respectively, which are consistent with our data. The time t_2 at which the amplitude F_2 appears is set by the inertio-capillary timescale τ_γ , independent of both the viscosity and the impact velocity of the drop. However, these properties dictate the magnitude of this amplitude.

Key words:

1. Introduction

Drop impacts have piqued the interest of scientists and artists alike for centuries, with the phenomenon being sketched by da Vinci (1508) in the early 16th and photographed by Worthington (1876a,b) in the late 19th century. It is, indeed, captivating to observe raindrops hitting a solid surface (Kim et al. 2020; Lohse & Villermaux 2020) or ocean spray affecting maritime structures (Berny et al. 2021; Villermaux et al. 2022). The phenomenology of drop impact is extremely rich, encompassing behaviors such as drop

† Email address for correspondence: vatsalsanjay@gmail.com

‡ Email address for correspondence: binzhang0710@mail.tsinghua.edu.cn

¶ Email address for correspondence: cunjinglv@mail.tsinghua.edu.cn

|| Email address for correspondence: d.lohse@utwente.nl

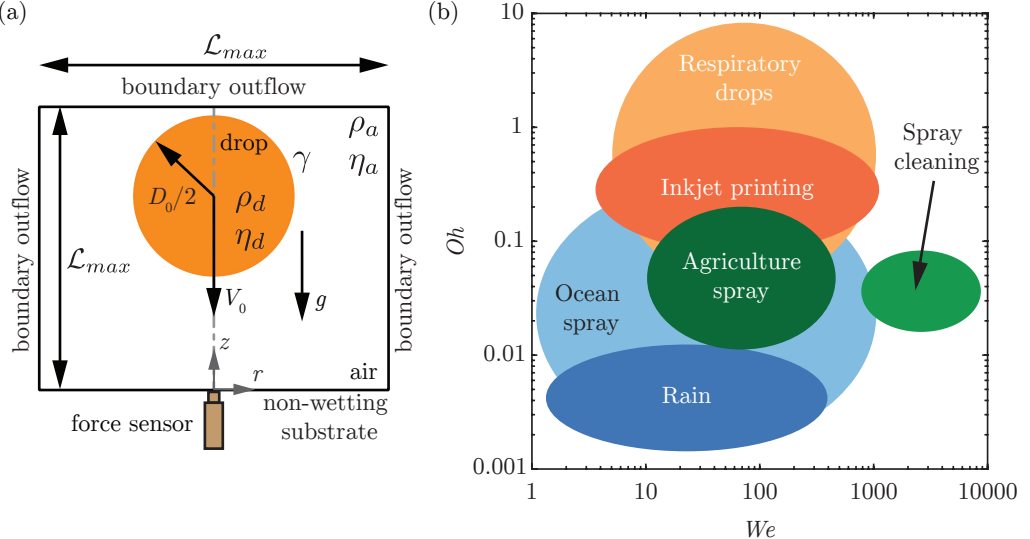


FIGURE 1. (a) Problem schematic with an axisymmetric computational domain used to study the impact of a drop with diameter D_0 and velocity V_0 on a non-wetting substrate. In the experiments, we use a quartz force sensor to measure the temporal variation of the impact force. The subscripts d and a denote the drop and air, respectively, to distinguish their material properties, which are the density ρ and the dynamic viscosity η . The drop-air surface tension coefficient is γ . The grey dashed-dotted line represents the axis of symmetry, $r = 0$. Boundary air outflow is applied at the top and side boundaries (tangential stresses, normal velocity gradient, and ambient pressure are set to zero). The domain boundaries are far enough from the drop not to influence its impact process ($L_{\max} \gg D_0$, $L_{\max} = 8R$ in the worst case). (b) The phase space with control parameters: the Weber number (We : dimensionless kinetic energy) and the Ohnesorge number (Oh : dimensionless viscosity), exemplifying different applications.

deformation (Biance *et al.* 2006; Moláček & Bush 2012; Chevy *et al.* 2012), spreading (Laan *et al.* 2014; Wildeman *et al.* 2016), splashing (Xu *et al.* 2005; Riboux & Gordillo 2014; Thoraval *et al.* 2021), fragmentation (Villermaux & Bossa 2011; Villermaux 2020), bouncing (Richard & Quéré 2000; Kolinski *et al.* 2014; Jha *et al.* 2020; Chubynsky *et al.* 2020; Sharma & Dixit 2021; Sanjay *et al.* 2023a), and wetting (de Gennes 1985; Fukai *et al.* 1995; Quéré 2008; Bonn *et al.* 2009). These behaviors are influenced by the interplay of inertial, capillary, and viscous forces, as well as additional factors like non-Newtonian properties (Bartolo *et al.* 2005, 2007; Smith & Bertola 2010; Gorin *et al.* 2022) of the liquid and even ambient air pressure (Xu *et al.* 2005), making the parameter space for this phenomenon both extensive and high-dimensional.

Naturally, even the process of a Newtonian liquid drop impacting a rigid substrate is governed by a plethora of control parameters, including but not limited to the drop's density ρ_d , diameter D_0 , velocity V_0 , dynamic viscosity η_d , surface tension γ , and acceleration due to gravity g (figure 1a). To navigate this rich landscape, we focus on two main dimensionless numbers that serve as control parameters (figure 1b): the Weber number We , which is the ratio of inertial to capillary forces and is given by

$$We = \frac{\rho_d V_0^2 D_0}{\gamma}, \quad (1.1)$$

and the Ohnesorge number Oh , which captures the interplay between viscous damping

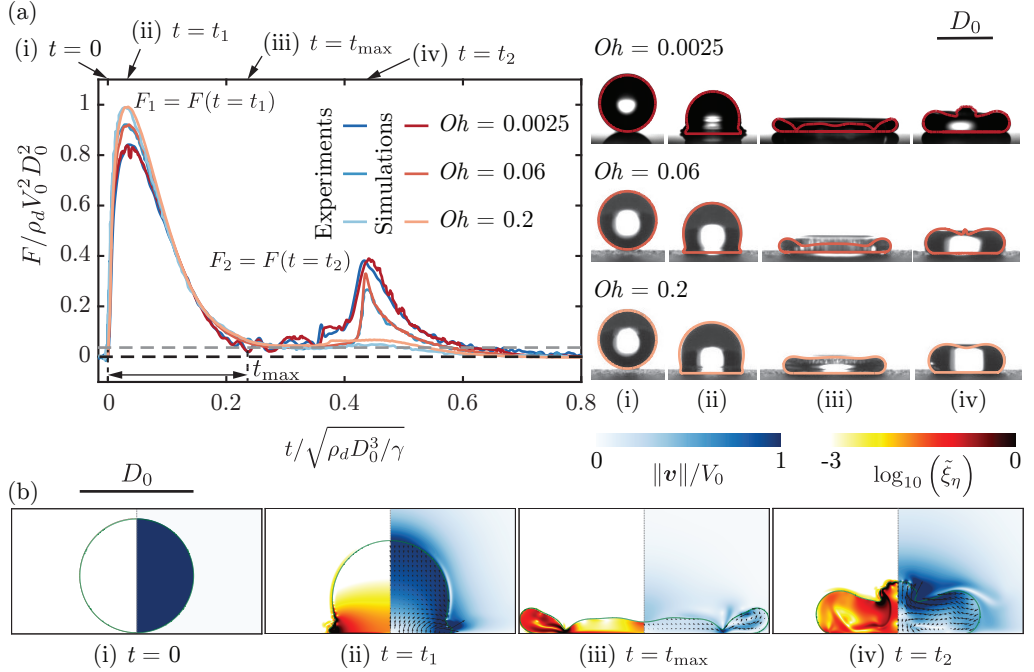


FIGURE 2. Comparison of the drop impact force $F(t)$ obtained from experiments and simulations for the three typical cases with impact velocity $V_0 = 1.2 \text{ m/s}, 0.97 \text{ m/s}, 0.96 \text{ m/s}$, diameter $D_0 = 2.05 \text{ mm}, 2.52 \text{ mm}, 2.54 \text{ mm}$, surface tension $\gamma = 72 \text{ mN/m}, 61 \text{ mN/m}, 61 \text{ mN/m}$ and viscosity $\eta_d = 1 \text{ mPa s}, 25.3 \text{ mPa s}, 80.2 \text{ mPa s}$. These parameter give $Oh = 0.0025, 0.06, 0.2$ and $We = 40$. For the three cases, the two peak amplitudes, $F_1/\rho_d V_0^2 D_0^2 \approx 0.82, 0.92, 0.99$ at $t_1 \approx 0.03\sqrt{\rho_d D_0^3/\gamma}$ and $F_2/\rho_d V_0^2 D_0^2 \approx 0.37, 0.337, 0.1$ at $t_2 \approx 0.42\sqrt{\rho_d D_0^3/\gamma}$, characterize the inertial shock from impact and the Worthington jet before takeoff, respectively. The drop reaches the maximum spreading at t_{\max} when it momentarily stops and retracts until $0.8\sqrt{\rho_d D_0^3/\gamma}$ when the drop takes off ($F = 0$). The black and gray dashed lines in panel (a) mark $F = 0$ and the resolution $F = 0.5 \text{ mN}$ of our piezoelectric force transducer, respectively. (b) Four instances are further elaborated through numerical simulations for ($We = 40, Oh = 0.0025$), namely (i) $t = 0 \text{ ms}$ (touch-down), (ii) $t = 0.37 \text{ ms}$ (t_1), (iii) $t = 2.5 \text{ ms}$ (t_{\max}), and (iv) $t = 4.63 \text{ ms}$ (t_2). The insets of panel (a) exemplify these four instances for the three representative cases illustrated here. The experimental snapshots are overlaid with the drop boundaries from simulations. We stress the excellent agreement between experiments and simulations without any free parameters. The left part of each numerical snapshot shows the dimensionless local viscous dissipation function $\tilde{\xi}_\eta \equiv \xi_\eta D_0 / (\rho_d V_0^3) = 2Oh (\tilde{\mathcal{D}} : \tilde{\mathcal{D}})$, where, \mathcal{D} is the symmetric part of the velocity gradient tensor, on a \log_{10} scale and the right part the velocity field magnitude normalized with the impact velocity. The black velocity vectors are plotted in the center of mass reference frame of the drop to clearly elucidate the internal flow. Also see supplementary videos SM1-SM3.

and capillary oscillations, offering insights into how viscosity affects the drop's behavior upon impact,

$$Oh = \frac{\eta_d}{\sqrt{\rho_d \gamma D_0}}. \quad (1.2)$$

Additionally, the Bond number

$$Bo = \frac{\rho_d g D_0^2}{\gamma} \quad (1.3)$$

57 compares gravity to inertial forces and is needed to uniquely define the non-dimensional
 58 problem.

59 The drop impact is not only interesting from the point of view of fundamental research
 60 but also finds relevance in inkjet printing (Lohse 2022), the spread of respiratory drops
 61 carrying airborne microbes (Bourouiba 2021; Ji *et al.* 2021; Pöhlker *et al.* 2023), cooling
 62 applications (Kim 2007; Shiri & Bird 2017; Jowkar & Morad 2019), agriculture (Bergeron
 63 *et al.* 2000; Bartolo *et al.* 2007; Kooij *et al.* 2018; Sijs & Bonn 2020; He *et al.* 2021;
 64 Hoffman *et al.* 2021), criminal forensics (Smith *et al.* 2018; Smith & Brutin 2018), and
 65 many other industrial and natural processes (Rein 1993; Yarin 2006; Tuteja *et al.* 2007;
 66 Cho *et al.* 2016; Josserand & Thoroddsen 2016; Yarin *et al.* 2017; Liu *et al.* 2017; Hao
 67 *et al.* 2016; Yarin *et al.* 2017; Wu *et al.* 2020). For these applications, it is pertinent to
 68 understand the forces involved in drop impacts, as these forces can lead to soil erosion
 69 (Nearing *et al.* 1986) or damage to engineered surfaces (Ahmad *et al.* 2013; Amirzadeh
 70 *et al.* 2017; Gohardani 2011). We refer the readers to Cheng *et al.* (2022) for an overview
 71 of the recent studies unraveling drop impact forces; see also Li *et al.* (2014); Soto *et al.*
 72 (2014); Philippi *et al.* (2016); Zhang *et al.* (2017); Gordillo *et al.* (2018); Mitchell *et al.*
 73 (2019); Zhang *et al.* (2019).

74 These forces have been studied by Zhang *et al.* (2022), employing experiments and
 75 simulations and deriving scaling laws. A liquid drop impacting a non-wetting substrate
 76 undergoes a series of phases—spreading, recoiling, and potentially rebounding (Chantelot
 77 2018)—driven by the normal reaction force exerted by the substrate (figure 2). The
 78 moment of touch-down (see figures 2a,b $t = 0$ to t_1) (Wagner 1932; Philippi *et al.*
 79 2016; Gordillo *et al.* 2018) is not surprisingly associated with a pronounced peak in
 80 the temporal evolution of the drop impact force $F(t)$ owing to the sudden deceleration
 81 as high as 100 times the acceleration due to gravity (Clanet *et al.* 2004) (figure 2a,
 82 $F(t = 0.37\text{ ms}) \approx 5.1\text{ mN}$). The force diminishes as the drop reaches its maximum
 83 spreading diameter (figure 2a,b $t = t_m$). Zhang *et al.* (2022) revealed that also the
 84 jump-off is accompanied by a peak in the normal reaction force, which was up to then
 85 unknown (figure 2a, $F_2(t_2 = 4.63\text{ ms}) \approx 2.3\text{ mN}$ for the second force peak amplitude—at
 86 time t_2 after impact). The second peak in the force also coincides with the formation of a
 87 Worthington jet, a narrow upward jet of liquid that can form due to flow focusing by the
 88 retracting drop (figure 2a,b $t = t_2$). Under certain conditions ($We \approx 9$), this peak can be
 89 even more pronounced than the first. This discovery is critical for superhydrophobicity
 90 which is volatile and can fail due to external disturbances such as pressure (Lafuma &
 91 Quéré 2003; Callies & Quéré 2005; Sbragaglia *et al.* 2007; Li *et al.* 2017), evaporation
 92 (Tsai *et al.* 2010; Chen *et al.* 2012; Papadopoulos *et al.* 2013), mechanical vibration
 93 (Bormashenko *et al.* 2007), or the impact forces of prior droplets (Bartolo *et al.* 2006a).

94 In contrast to our prior study Zhang *et al.* (2022), which fixed the Ohnesorge number
 95 to that of a 2 mm diameter water drop ($Oh = 0.0025$), our present investigation reported
 96 in this paper explores a broader parameter space. We systematically and independently
 97 vary the Weber and Ohnesorge numbers, extending the range of Oh to as high as 100.
 98 This comprehensive approach enables us to develop new scaling laws and provides a
 99 more unified understanding of the forces involved in drop impact problems. Our findings
 100 are particularly relevant for applications with varying viscosities and impact velocities
 101 (figure 1).

102 The structure of this paper is as follows: §2 briefly describes the experimental and
 103 numerical methods. §3 and §4 offer detailed analyses of the first and second peaks,
 104 respectively, focusing on their relationships with the Weber number (We) and the
 105 Ohnesorge number (Oh). Conclusions and perspectives for future research are presented
 106 in Section 5.

glycerol (wt %)	ρ_d (kg/m ³)	η_d (mPa.s)	γ (mN/m)
0	1000	1	72
50	1124	5	61
63	1158	10	61
74	1188	25.3	61
80	1200	45.4	61
85	1220	80.2	61

TABLE 1. Properties of the water-glycerol mixtures used in the experiments. ρ_d and η_d are the density and viscosity of the drop, respectively and γ denotes the liquid-air surface tension coefficient. These properties are calculated using the protocol provided in Cheng (2008); Volk & Kähler (2018).

2. Methods

2.1. Experimental method

In the experimental setup, shown schematically in figure 1(a), a liquid drop impacts a superhydrophobic substrate. For water drops, such a surface is coated with silanized silica nanobeads with a diameter of 20 nm (Glaco Mirror Coat Zero; Soft99) resulting in the advancing and receding contact angles of $167 \pm 2^\circ$ and $154 \pm 2^\circ$, respectively (Gauthier *et al.* 2015; Li *et al.* 2017). On the other hand, for viscous aqueous glycerin drops, the upper surface is coated with an acetone solution of hydrophobic beads (Ultra ever Dry, Ultratech International, a typical bead size of 20 nm), resulting in the advancing and receding contact angles of $166 \pm 4^\circ$ and $159 \pm 2^\circ$, respectively (Jha *et al.* 2020). The properties of the impacting drop are controlled using water-glycerol mixtures with viscosities η_d varying by almost two orders of magnitude, from 1 mPas to 80.2 mPas. Surface tension is either 72 mN/m (pure water) or 61 mN/m (glycerol), while density ρ_d ranges from 1000 kg/m³ to 1220 kg/m³, as detailed in table 1 (Cheng 2008; Volk & Kähler 2018; Jha *et al.* 2020). We note that using liquids such as silicone oil can provide a broader range of viscosity variation when paired with a superamphiphobic substrate (Deng *et al.* 2012). Additionally, employing drops of smaller radii facilitates the exploration of higher Ohnesorge numbers (Oh , see (1.2)). The drop diameter D_0 is controlled between 2.05 mm and 2.76 mm by pushing it through a calibrated needle (see appendix A for details). Consequently, we calculate Oh using the properties in table 1. The Weber number (We , see (1.1)) is set using the impact velocity V_0 varying between 0.38 m/s and 2.96 m/s by changing the release height of the drops above the substrate. All experiments are conducted at ambient pressure and temperature. The impact force is directly measured using a high-precision piezoelectric force transducer (Kistler 9215A) with a resolution of 0.5 mN. During these measurements, the high-frequency vibrations induced by the measurement system and the surrounding noise are spectrally removed using a low pass filter with a cut-off frequency of 5 kHz, following the procedure in Li *et al.* (2014); Zhang *et al.* (2017); Gordillo *et al.* (2018); Mitchell *et al.* (2019). The experiment also employs a high-speed camera (Photron Fastcam Nova S12) synchronized at 10,000 fps with a shutter speed 1/20,000 s. Throughout the manuscript, the error bars account for repeated trials and are visible if they are larger than the marker size. We refer the readers to the supplementary material of Zhang *et al.* (2022) and appendix A for further details of the experimental setup and error characterization of the dimensionless control parameters, respectively.

R2

R2

141 2.2. Numerical framework

142 In the direct numerical simulations (DNS) employed for this study, the continuity and
 143 the momentum equations take the form

$$\nabla \cdot \mathbf{v} = 0 \quad (2.1)$$

144 and

$$\frac{\partial \mathbf{v}}{\partial t} + \nabla \cdot (\mathbf{v} \mathbf{v}) = \frac{1}{\rho} (-\nabla p + \nabla \cdot (2\eta \mathcal{D}) + \mathbf{f}_\gamma) + \mathbf{g}, \quad (2.2)$$

145 respectively. Here, \mathbf{v} is the velocity field, t is time, p is pressure, and \mathbf{g} is acceleration
 146 due to gravity. We use the free software program *Basilisk C* that employs the well-
 147 balanced geometric volume of fluid (VoF) method (Popinet 2009, 2018). The VoF tracer
 148 Ψ delineates the interface between the drop (subscript d , $\psi = 1$) and air (subscript a ,
 149 $\psi = 0$), introducing a singular force $\mathbf{f}_\gamma \approx \gamma\kappa\nabla\Psi$ (κ denotes interfacial curvature, see
 150 Brackbill *et al.* 1992) to respect the dynamic boundary condition at the interface. This
 151 VoF tracer sets the material properties such that density ρ and viscosity η are given by

$$\rho = \rho_a + (\rho_d - \rho_a)\Psi \quad (2.3)$$

152 and

$$\eta = \eta_a + (\eta_d - \eta_a)\Psi, \quad (2.4)$$

153 respectively. This VoF field is advected with the flow, following the equation

$$\frac{\partial \Psi}{\partial t} + \nabla \cdot (\mathbf{v}\Psi) = 0. \quad (2.5)$$

154 Lastly, we calculate the normal reaction force $\mathbf{F}(t)$ by integrating the pressure field p at
 155 the substrate,

$$\mathbf{F}(t) = \left(\int_{\mathcal{A}} (p - p_0) d\mathcal{A} \right) \hat{\mathbf{z}}, \quad (2.6)$$

156 where, p_0 , $d\mathcal{A}$, and $\hat{\mathbf{z}}$ are the ambient pressure, substrate area element, and the unit
 157 vector normal to the substrate, respectively.

158 We leverage the axial symmetry of the drop impact (figure 1a). This axial symmetry
 159 breaks at large We (≥ 100 for water drops and even larger Weber number for more
 160 viscous drops), owing to destabilization by the surrounding gas after splashing (Xu *et al.*
 161 2005; Eggers *et al.* 2010; Driscoll & Nagel 2011; Riboux & Gordillo 2014; Josserand &
 162 Thoroddsen 2016; Zhang *et al.* 2022). To solve the governing equations (2.1)-(2.5), the
 163 velocity field \mathbf{v} and time t are normalized by the inertio-capillary scales, $V_\gamma = \sqrt{\gamma/\rho_d D_0}$
 164 and $\tau_\gamma = \sqrt{\rho_d D_0^3/\gamma}$, respectively. Furthermore, the pressure is normalized using the
 165 capillary pressure scale $p_\gamma = \gamma/D_0$. In such a conceptualization, Oh and We described in
 166 §1 uniquely determine the system. The Ohnesorge number based on air viscosity $Oh_a =$
 167 $(\eta_a/\eta_d)Oh$ and air-drop density ratio ρ_a/ρ_d are fixed at 10^{-5} and 10^{-3} , respectively
 168 to minimize the influence of the surrounding medium on the impact forces. Lastly, we R2
 169 keep the Bond number (Bo , see (1.3)) fixed at 1 throughout the manuscript. In our

system, the relevance of gravity is characterized by the dimensionless Froude number $Fr = V_0^2/gD_0 = We/Bo$ comparing inertia with gravity. Throughout this manuscript, $Fr > 1$ and gravity's role is sub-dominant compared to inertia (for detailed discussion, see appendix B). The substrate is modeled as a no-slip and non-penetrable wall, whereas vanishing stress and pressure are applied at the remaining boundaries to mimic outflow conditions for the surrounding air. The domain boundaries are far enough from the drop not to influence its impact process ($\mathcal{L}_{\max} \gg D_0$, $\mathcal{L}_{\max} = 8R$ in the worst case). At $t = 0$, in our simulations, we release a spherical drop whose south pole is $0.05D_0$ away from the substrate and is falling with a velocity V_0 . It is important to note that experimental drops may deviate from perfect sphericity due to air drag as they fall after detaching from the needle and potential residual oscillations from detachment. These shape perturbations are more pronounced in cases with low Weber and Ohnesorge numbers. To quantify this non-sphericity, we measure the drop's aspect ratio (horizontal to vertical diameter) immediately before substrate contact. The precise pre-impact drop shape can significantly influence subsequent impact dynamics (Thoraval *et al.* 2013; Yun 2017; Zhang *et al.* 2019). In our experiments, we constrain our analysis to drops with aspect ratios between 0.96 and 1.05. Given this narrow range, we posit that the impact of these shape variations is negligible compared to the experimental error bars derived from repeated trials under identical nominal conditions. The simulations utilize adaptive mesh refinement to finely resolve the velocity, viscous dissipation, and the VoF tracer fields. A minimum grid size $\Delta = D_0/2048$ is used for this study.

To ensure a perfectly non-wetting surface, we impose a thin air layer (minimum thickness $\sim \Delta/2$) between the drop and the substrate. This air layer prevents direct contact between the liquid and solid (Kolinski *et al.* 2014; Sprittles 2024), effectively mimicking a perfectly non-wetting surface. The presence of this air layer is crucial for capturing the dynamics of drop impact on superhydrophobic surfaces, as it allows for the formation of an air cushion that can significantly affect the spreading and rebound behavior of the drop (Ramírez-Soto *et al.* 2020; Sanjay *et al.* 2023a). While this approach does not fully resolve the microscopic dynamics within the air layer itself, such as the high-velocity gradients and viscous dissipation inside the gas film once it thins below a critical size ($\sim 10\Delta$), it has been shown to accurately capture the macroscopic behavior of drop impact in the parameter range of interest (Ramírez-Soto *et al.* 2020; Sanjay *et al.* 2023b; Alventosa *et al.* 2023a; García-Geijo *et al.* 2024). We refer the readers to Sanjay (2022) for discussions about this “precursor”, air film method and to Popinet & collaborators (2013–2023); Sanjay (2024); Zhang *et al.* (2022) for details on the numerical framework.

3. Anatomy of the first impact force peak

This section elucidates the anatomy of the first impact force peak and its relationship with the Weber We and Ohnesorge Oh numbers, first for the inertial limit (§3.1, $Oh \ll 1$) and then for the viscous asymptote (§3.2, $Oh \gg 1$). The results of this section are summarized in figure 3 that shows an excellent agreement between experiments and simulations without any free parameters.

3.1. Low Ohnesorge number impacts

For low Oh and large We , inertial force and time scales dictate the drop impact dynamics (figures 3 and 4). As the drop falls on a substrate, the part of the drop immediately in contact with the substrate stops moving, whereas the top of the drop

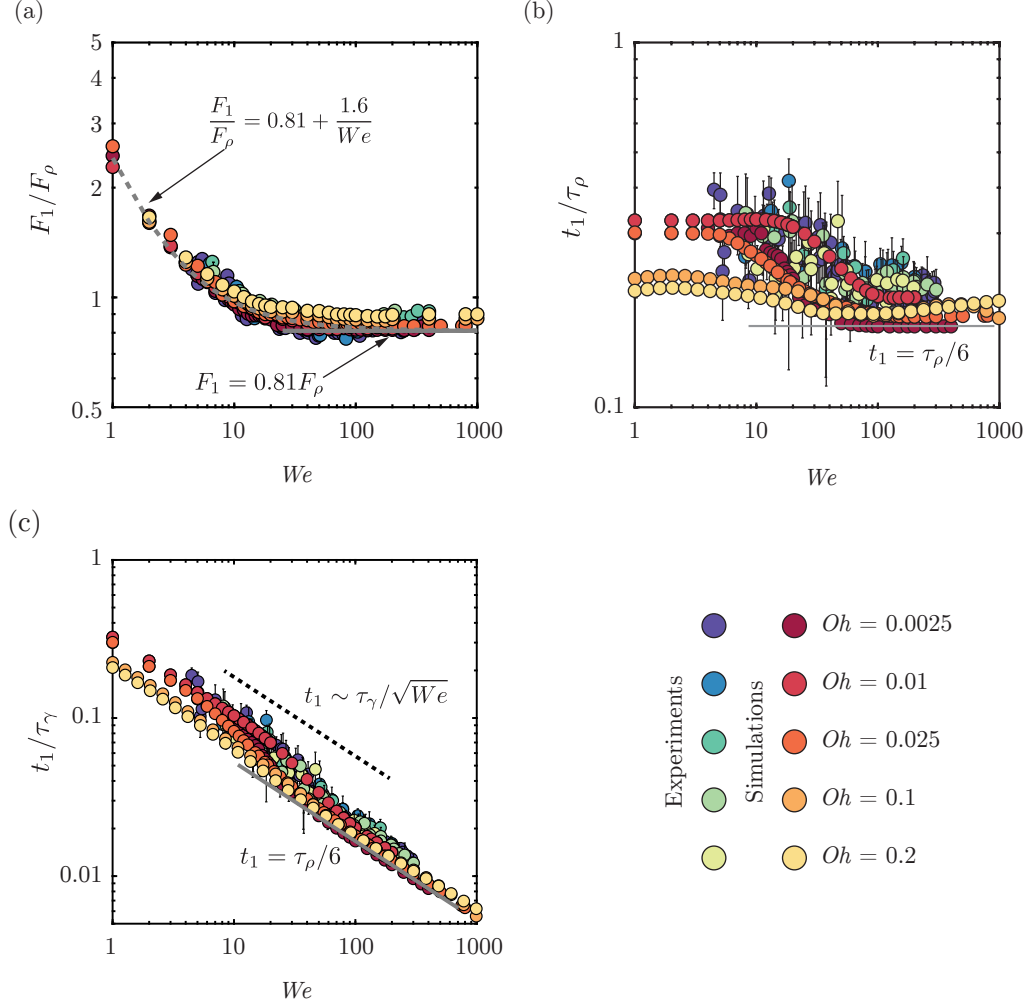


FIGURE 3. Anatomy of the first impact force peak amplitude at low Oh in between 0.0025 and 0.2, see color legend: We dependence of the (a) magnitude F_1 normalized by the inertial force scale $F_\rho = \rho_d V_0^2 D_0^2$ and time t_1 to reach the first force peak amplitude normalized by (b) the inertial timescale $\tau_\rho = D_0/V_0$ and (c) the inertia-capillary time scale $\tau_\gamma = \sqrt{\rho_d D_0^3/\gamma}$.

216 still falls with the impact velocity (figure 4, from $t = t_1/4$ until $t = t_1$). Consequently,
 217 momentum conservation implies

$$F_1 \sim V_0 \frac{dm}{dt}, \quad (3.1)$$

218 where the mass flux $dm/dt \sim \rho_d V_0 D_0^2$ (Soto *et al.* 2014; Zhang *et al.* 2022). As a result,
 219 the first peak amplitude scales with the inertial pressure force (figure 3a)

$$F_1 \sim F_\rho, \text{ where } F_\rho = \rho_d V_0^2 D_0^2, \quad (3.2)$$

220 for high Weber numbers ($We > 30$, $F_1 \approx 0.81F_\rho$). Furthermore, the time t_1 to reach F_1
 221 follows

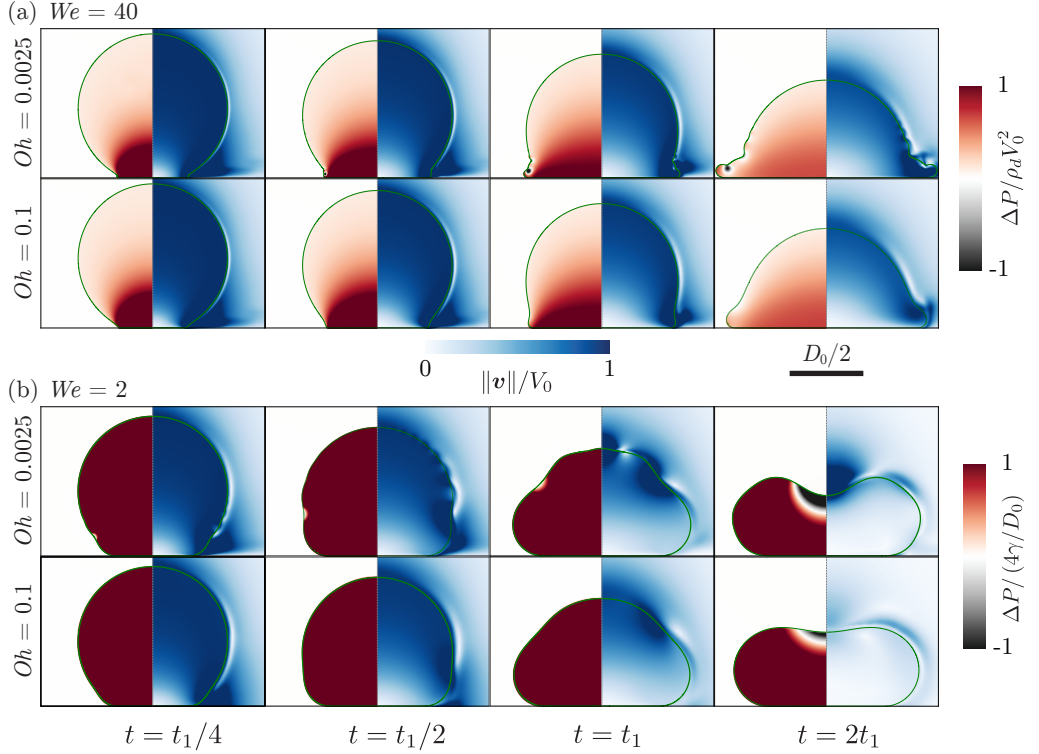


FIGURE 4. Direct numerical simulations snapshots illustrating the drop impact dynamics for $We =$ (a) 40 and (b) 2. The left-hand side of each numerical snapshot shows the pressure normalized by (a) the inertial pressure scale $\rho_d V_0^2$ and (b) the capillary pressure scale γ/D_0 . The right-hand side shows the velocity field magnitude normalized by the impact velocity V_0 .

$$t_1 \sim \frac{D_0}{V_0} = \tau_\rho, \quad (3.3)$$

where, τ_ρ is the inertial timescale. The relation between equations (3.2) and (3.3) is apparent from the momentum conservation which implies that the impulse of the first force peak is equal to the momentum of the impacting drop, i.e., $F_1 t_1 \sim \rho_d V_0 D_0^3 = F_\rho \tau_\rho$ (see Gordillo *et al.* 2018, Zhang *et al.* 2022, and figures 3b,c). These scaling laws depend only on the inertial shock at impact and are wettability-independent (Zhang *et al.* 2017; Gordillo *et al.* 2018; Zhang *et al.* 2022). For details of the scaling law, including the prefactors, we refer the readers to Philippi *et al.* (2016); Gordillo *et al.* (2018); Cheng *et al.* (2022).

Figure 3 further illustrates that this inertial asymptote is insensitive to viscosity variations up to 100-fold as $F_1 \sim F_\rho$ and $t_1 \sim \tau_\rho$ for $0.0025 < Oh < 0.2$. However, deviations from the inertial force and time scales are apparent for $We < 30$ (figure 3), a phenomenon also reported in earlier work (Soto *et al.* 2014; Zhang *et al.* 2022). In these instances, inertia does not act as the sole governing force but instead complements surface tension, which dictates the pressure inside the drop ($p \sim \gamma/D_0$ throughout the drop for $We \lesssim 1$, figure 4b). Zhang *et al.* (2022) proposed an empirical functional dependence as

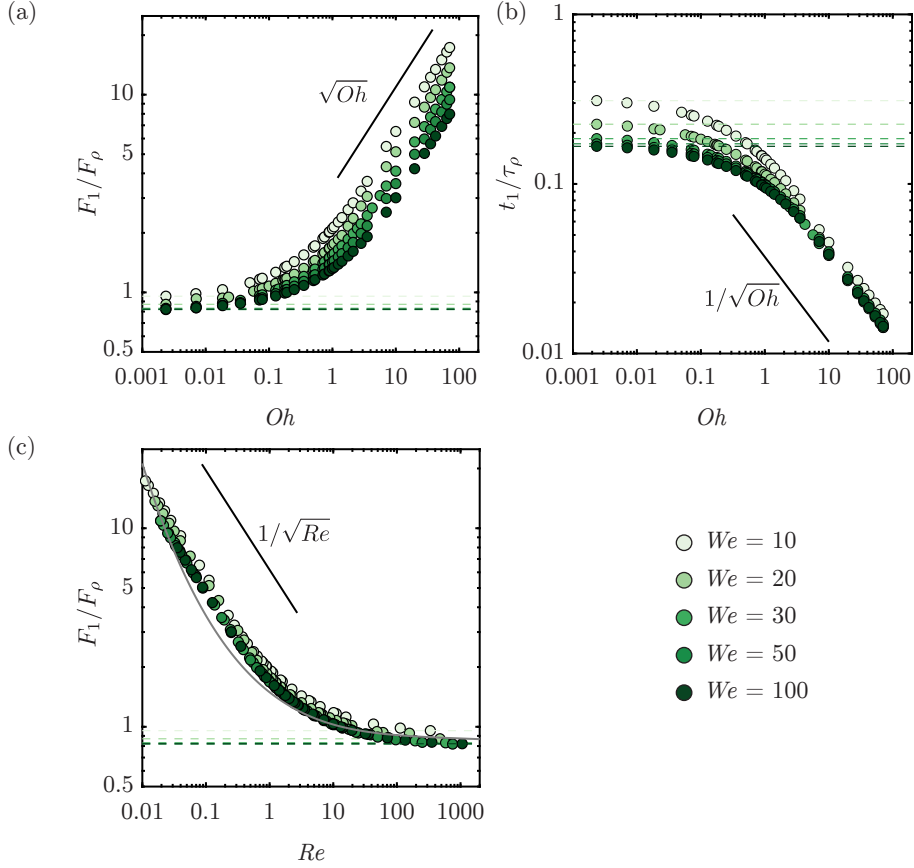


FIGURE 5. Anatomy of the first impact force peak amplitude for viscous impacts from our numerical simulations: the Oh dependence of (a) the magnitude F_1 normalized by the inertial force scale $\rho_d V_0^2 D_0^2$ and (b) the time t_1 to reach the first force peak amplitude normalized by inertial timescale $\tau_\rho = D_0/V_0$. (c) The Re dependence of the magnitude F_1 normalized by the inertial force scale $\rho_d V_0^2 D_0^2$ as compared to the (implicit) theoretical calculation of Gordillo *et al.* (2018). The black line corresponds to the scaling relationship described in §3.2. The Weber number is color-coded.

$$F_1 = \left(\alpha_1 \rho_d V_0^2 + \alpha_2 \frac{\gamma}{D_0} \right) D_0^2, \quad (3.4)$$

based on dimensional analysis, with α_1 and α_2 as free parameters which were determined to be approximately 1.6 and 0.81, respectively for water ($Oh = 0.0025$). These coefficients only deviate marginally in the current work despite the significant increase in Oh as compared to previous works (Cheng *et al.* 2022; Zhang *et al.* 2022). This consistency underscores the invariance of the pressure field inside the drop to an increase in Oh (close to the impact region, figure 4a and throughout the drop, figure 4b).

3.2. Large Ohnesorge number impacts

Figure 5 reaffirms the findings of §3.1 for low Oh that the first impact peak amplitude F_1 and the time to reach this peak amplitude t_1 scale with F_ρ and τ_ρ , respectively. As the Ohnesorge number increases further, the first impact force peak amplitude normalized

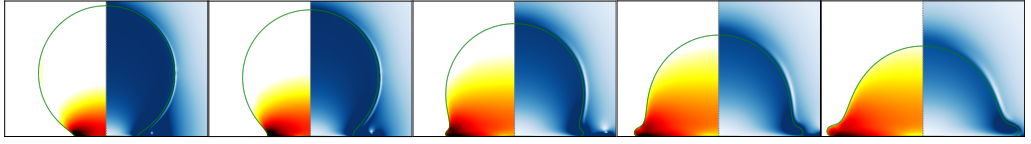
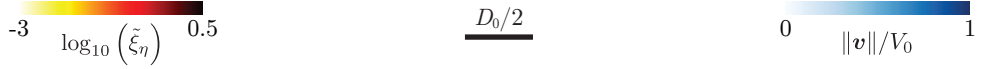
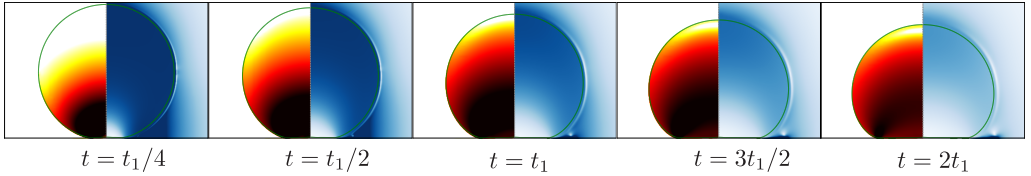
(a) $Oh = 0.05$ (b) $Oh = 0.5$ (c) $Oh = 5$ 

FIGURE 6. Direct numerical simulations snapshots illustrating the drop impact dynamics for $We = 100$ and $Oh =$ (a) 0.05 , (b) 0.5 , and (c) 5 . The left-hand side of each numerical snapshot shows the viscous dissipation function ξ_η normalized by the inertial scale $\rho_d V_0^3 / D_0$. The right-hand side shows the velocity field magnitude normalized by the impact velocity V_0 .

with F_ρ begins to increase, indicating a transition around $Oh \approx 0.1$, where viscosity starts to play a significant role. At large Oh , we observe the scaling relationship (figure 5a)

$$F_1 \sim F_\rho \sqrt{Oh}. \quad (3.5)$$

The drop's momentum is still $\rho_d V_0 D_0^3$ which must be balanced by the impulse from the substrate, $F_1 t_1$ (see §3.1, Gordillo *et al.* 2018, Zhang *et al.* 2022, and figure 5b). Consequently, the time t_1 follows

$$t_1 \sim \frac{\tau_\rho}{\sqrt{Oh}}. \quad (3.6)$$

Figure 5 further shows that these scaling laws are weakly dependent on the Weber number, as viscous dissipation consumes the entire initial kinetic energy of the impacting drop (figure 6). Once again, we stress that using the water-glycerol mixtures limits the range of Oh that we can probe experimentally. We further note that the first peak is robust and does not depend on the wettability of the substrate. Consequently, to compare with the existing data such as those in Cheng *et al.* (2022) with different liquids to cover a wider range of liquid viscosities and to account for the apparent We -dependence, we plot F_1 compensated with F_ρ against the impact Reynolds number $Re \equiv \sqrt{We}/Oh = V_0 D_0 / \nu_d$. For the low Re regime, such a plot allows us to describe the We dependence on the prefactor more effectively, as illustrated in figure 5(c). However, it is important to note that some scatter is still observed at high Re values, which can be attributed to the We dependence of the impact force peak amplitude. This lack of a pure scaling behavior

demonstrates how the interplay between kinetic energy and viscous dissipation within the drop dictates the functional dependence of the maximum impact force on Oh .

To systematically elucidate these scaling behaviors in the limit of small Re , we need to find the typical scales for the rate of change of kinetic energy and that of the rate of viscous dissipation for the drop impact system. First, we can readily define an average rate of viscous dissipation per unit mass as

$$\bar{\varepsilon} \sim \frac{1}{\tau_\rho} \frac{1}{D_0^3} \int_0^{\tau_\rho} \int_{\Omega} \nu_d (\mathcal{D} : \mathcal{D}) d\Omega dt, \quad (3.7)$$

where ν_d is the kinematic viscosity of the drop and $d\Omega$ is the volume element where dissipation occurs. Notice that $\bar{\varepsilon}$ has the dimensions of V_0^3/D_0 , i.e., length squared over time cubed or velocity squared over time, as it should be for dissipation rate of energy per unit mass. We can estimate $\Omega = D_{\text{foot}}^2 l_\nu$ (figure 6), where D_{foot} is the drop's foot diameter in contact with the substrate and l_ν is the viscous boundary layer thickness. This boundary layer marks the region of strong velocity gradients ($\sim V_0/l_\nu$) analogous to the Mirels (1955) shockwave-induced boundary layer. For details, we refer the authors to Schlichting (1968); Schroll *et al.* (2010); Philippi *et al.* (2016). Consequently, the viscous dissipation rate scales as

$$\bar{\varepsilon} \sim \frac{1}{\tau_\rho D_0^3} \int_0^{\tau_\rho} \nu_d \left(\frac{V_0}{l_\nu} \right)^2 D_{\text{foot}}^2 l_\nu dt. \quad (3.8)$$

To calculate D_{foot} , we assume that the drop maintains a spherical cap shape throughout the impact (figure 6). To calculate the distance the drop would have traveled if there were no substrate, we use the relation $d \sim V_0 t$. Simple geometric arguments allow us to determine the relation between the foot diameter and this distance, $D_{\text{foot}} \sim \sqrt{D_0 d}$ (Lesser 1981; Mandre *et al.* 2009; Zheng *et al.* 2021; Bilotto *et al.* 2023; Bertin 2023). Interestingly, this scaling behavior is similar to the inertial limit (Wagner 1932; Bouwhuis *et al.* 2012; Philippi *et al.* 2016; Gordillo *et al.* 2019) as discussed by Langley *et al.* (2017); Bilotto *et al.* (2023). Furthermore, the viscous boundary layer l_ν can be approximated using $\sqrt{\nu_d t}$ (Mirels 1955; Eggers *et al.* 2010; Philippi *et al.* 2016). Filling these in (3.8), we get

$$\bar{\varepsilon} \sim \frac{1}{\tau_\rho D_0^2} \int_0^{\tau_\rho} \sqrt{\nu_d} V_0^3 \sqrt{t} dt, \quad (3.9)$$

which on integration gives

$$\bar{\varepsilon} \sim \sqrt{\nu_d \tau_\rho} V_0^3 / D_0^2, \quad (3.10)$$

where τ_ρ is the inertial time scale. Here, we assume that for highly viscous drops, all energy is dissipated within a fraction of τ_ρ . Filling in (3.10) and normalizing $\bar{\varepsilon}$ with the inertial scales V_0^3/D_0 ,

$$\frac{\bar{\varepsilon}}{V_0^3/D_0} \sim \sqrt{\frac{\nu_d \tau_\rho}{D_0^2}} = \frac{1}{\sqrt{Re}} = \left(\frac{Oh}{\sqrt{We}} \right)^{1/2}. \quad (3.11)$$

Next, the kinetic energy of the falling drop is given by

$$\dot{K}(t) \equiv \frac{dK(t)}{dt} \sim \rho_d D_0^3 \bar{\varepsilon}, \quad \text{where } K(t) = \frac{1}{2} m (V(t))^2, \quad (3.12)$$

294 and $V(t)$ is the drop's center of mass velocity. The left-hand side of (3.12) can be written
 295 as

$$\dot{K}(t) = mV(t) \frac{dV(t)}{dt} = F(t)V(t). \quad (3.13)$$

296 In equation (3.13), $F(t)$ and $V(t)$ scale with the first impact force peak amplitude F_1
 297 and the impact velocity V_0 , respectively, giving the typical scale of the rate of change of
 298 kinetic energy as

$$\dot{K}^* \sim F_1 V_0. \quad (3.14)$$

299 We stress that (3.14) states that the rate of change of kinetic energy is equal to the power
 300 of the normal reaction force, an observation already made by [Wagner \(1932\)](#) and [Philippi
 et al. \(2016\)](#) in the context of impact problems. Lastly, at large Oh , viscous dissipation
 302 enervates kinetic energy completely giving (figure 6c, also see: [Philippi et al. \(2016\)](#) and
 303 [Wildeman et al. \(2016\)](#)),

$$\dot{K}^* \sim F_1 V_0 \sim \rho_d D_0^3 \bar{\varepsilon} \quad (3.15)$$

304 Additionally, we use the inertial scales to non-dimensionalize (3.15) and fill in (3.11),
 305 giving

$$\frac{F}{F_\rho} \sim \frac{\bar{\varepsilon}}{V_0^3/D_0} \sim \frac{1}{\sqrt{Re}} = \left(\frac{Oh}{\sqrt{We}} \right)^{1/2} \quad (3.16)$$

306 and using $F_1 t_1 \sim \rho_d V_0 D_0^3 = F_\rho \tau_\rho$,

$$\frac{t_1}{\tau_\rho} \sim \left(\frac{\sqrt{We}}{Oh} \right)^{1/2}. \quad (3.17)$$

307 In summary, we use energy and momentum invariance to elucidate the parameter
 308 dependencies of the impact force as illustrated in figure 5. The scaling arguments
 309 capture the dominant force balance during the impact process, considering the relative
 310 importance of inertial, capillary, and viscous forces. As the dimensionless viscosity of
 311 impacting drops increases, the lack of surface deformation increases the normal reaction
 312 force (3.16). Further, the invariance of incoming drop momentum implies that this
 313 increase in normal reaction force occurs on a shorter timescale (3.17).

314 4. Anatomy of the second impact force peak

315 This section delves into the anatomy of the second impact force peak amplitude F_2 as a
 316 function of the Weber We and Ohnesorge Oh numbers, summarized in figure 7. We once
 317 again note the remarkable agreement between experiments and numerical simulations in
 318 this figure.

319 Similar to the mechanism leading to the formation of the first peak (§3), also the

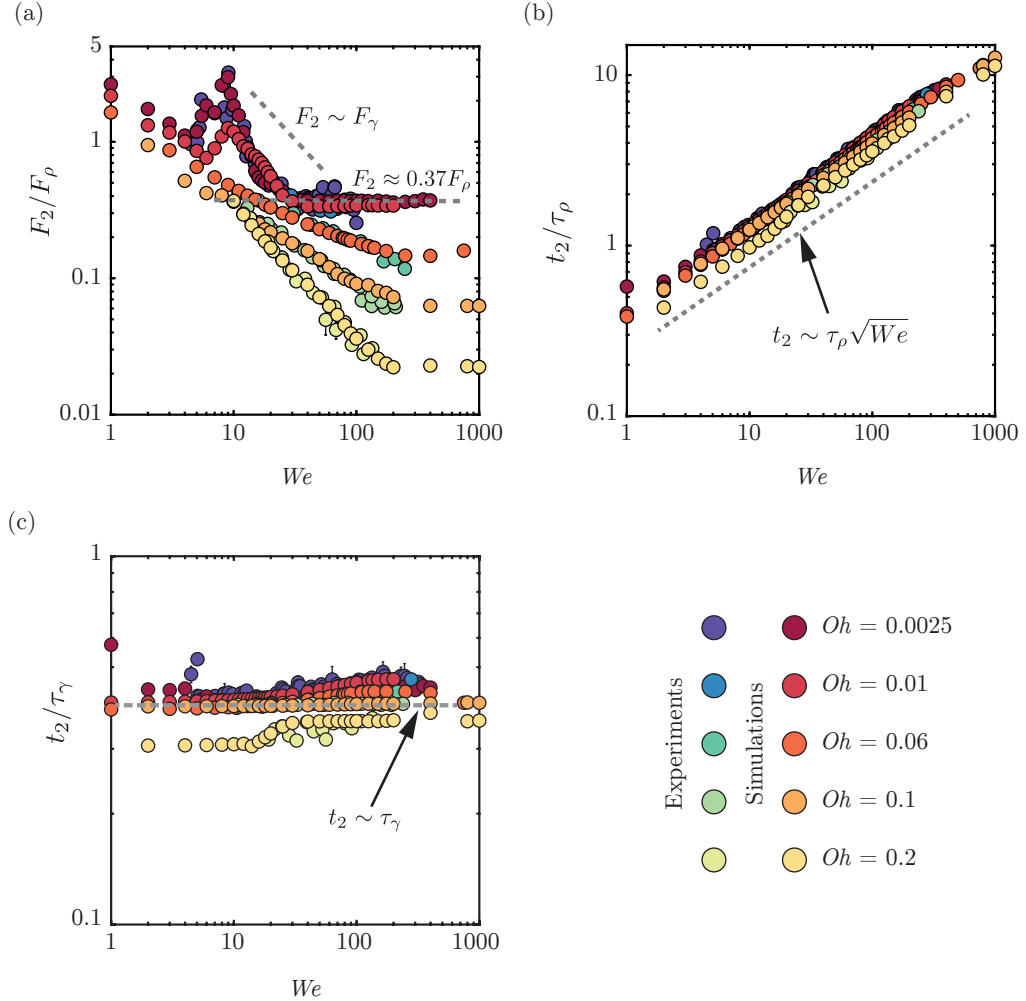


FIGURE 7. Anatomy of the second impact force peak amplitude: We dependence of the (a) magnitude F_2 normalized by the inertial force scale $F_\rho = \rho_d V_0^2 D_0^2$ and time t_2 to reach the second force peak amplitude normalized by (b) the inertio-capillary time scale $\tau_\gamma = \sqrt{\rho_d D_0^3 / \gamma}$ and (c) inertial timescale $\tau_\rho = D_0 / V_0$.

mechanism for the formation of this second peak is momentum conservation. As the drop takes off the surface, it applies a force on the substrate. As noted in §1 and Zhang *et al.* (2022), this force also coincides with the formation of a Worthington jet (figure 2iv). The time t_2 at which the second peak is observed scales with the inertio-capillary timescale and is insensitive to We and Oh (figure 7b,c). Once again, we invoke the analogy between drop oscillation and drop impact to explain this behavior (Richard *et al.* 2002; Chevy *et al.* 2012). At the time instant $t_2 \approx 0.44\tau_\gamma$, the drop's internal motion undergoes a transition from a predominantly radial flow to a vertical one due to the formation of the Worthington jet (Chantelot 2018; Zhang *et al.* 2022). Figure 8 exemplifies this jet in the Oh - We parameter space, which is intricately related to the second peak in the drop impact force. For low Oh and large We , the drop retraction follows a modified Taylor-Culick dynamics (Bartolo *et al.* 2005; Eggers *et al.* 2010; Sanjay *et al.* 2022). As We is

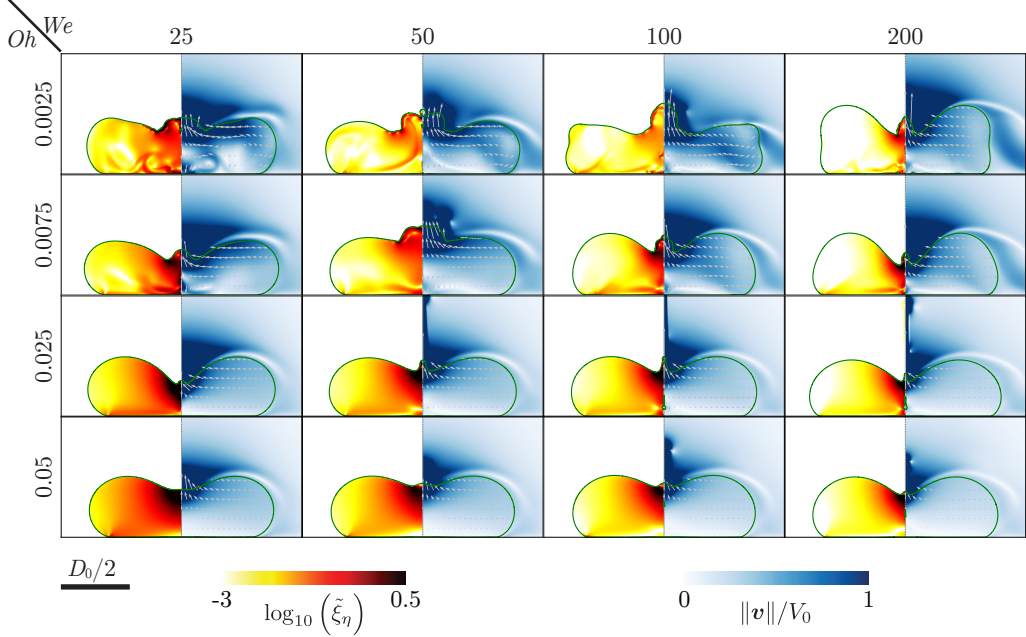


FIGURE 8. Direct numerical simulations snapshots illustrating the influence of We and Oh on the inception of the Worthington jet. All these snapshots are taken at the instant when the second peak appears in the temporal evolution of the normal reaction force ($t = t_2$). The left-hand side of each numerical snapshot shows the viscous dissipation function ξ_η normalized by the inertial scale $\rho_d V_0^3 / D_0$. The right-hand side shows the velocity field magnitude normalized by the impact velocity V_0 . The gray velocity vectors are plotted in the center of mass reference frame of the drop to clearly elucidate the internal flow.

increased, the jet gets thinner but faster, maintaining a constant momentum flux $\rho_d V_j^2 d_j^2$, where V_j and d_j are the jet's velocity and diameter, respectively (figure 8, Zhang *et al.* 2022). This invariance leads to the observed scaling $F_2 \sim F_\rho$ in this regime ($F_2 \approx 0.37 F_\rho$ for $We \geq 30, Oh \leq 0.01$).

Furthermore, the low We and Oh regime relies entirely on capillary pressure (figure 4). Subsequently, $F_2 \sim F_\gamma = \gamma D_0$ for $Oh < 0.01$ and $We < 30$ (figure 7). This flow focusing (figure 8) is most efficient for $We = 9$ (figure 9a, $t_2/2 < t < t_2$, Renardy *et al.* 2003; Bartolo *et al.* 2006b) where the capillary resonance leads to a thin-fast jet, accompanied by a bubble entrainment, reminiscent of the hydrodynamic singularity (figure 9, Zhang *et al.* 2022; Sanjay *et al.* 2021). The characteristic feature of this converging flow is a higher magnitude of F_2 compared to F_1 (figure 7).

However, this singular jet regime is very narrow in the Oh - We phase space. Figure 9b shows two cases for water drops ($Oh = 0.0025$) at different We (5 and 12 for figures 9b-i and b-ii, respectively). Bubble entrainment does not occur in either of these cases. Consequently, the maximum force amplitude diminishes for these two cases (figure 7). Nonetheless, these cases are still associated with high local viscous dissipation near the axis of symmetry owing to the singular nature of the flow. Another mechanism to inhibit this singular Worthington jet is viscous dissipation in the bulk. As the Ohnesorge number increases, this singular jet formation disappears ($Oh = 0.005$, figure 9c-i), significantly reducing the second peak of the impact force. For even higher viscosities, the drop no longer exhibits the sharp, focused jet formation seen at lower viscosities, and the second peak in the force is notably diminished ($Oh = 0.05$, figure 9c-ii).

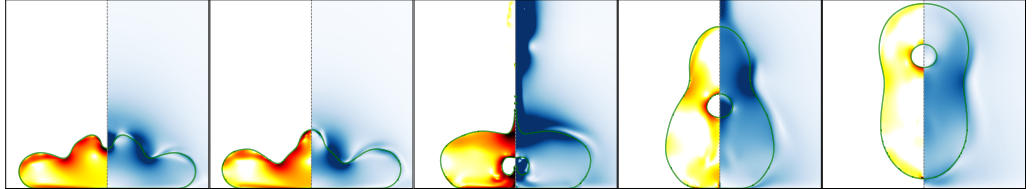
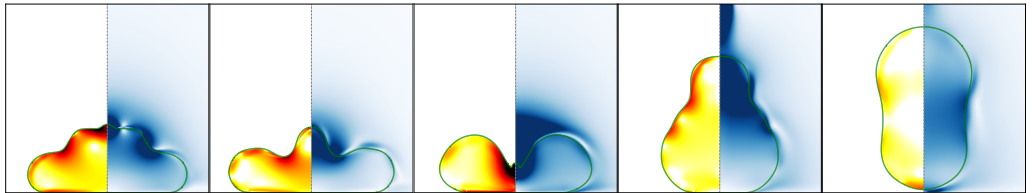
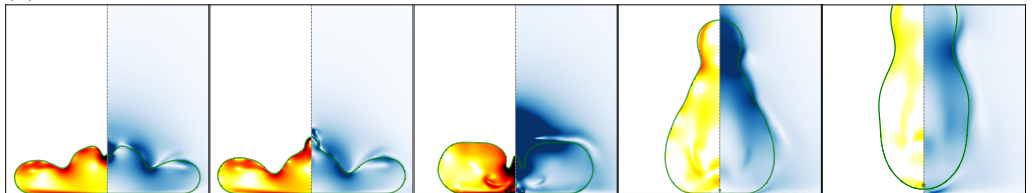
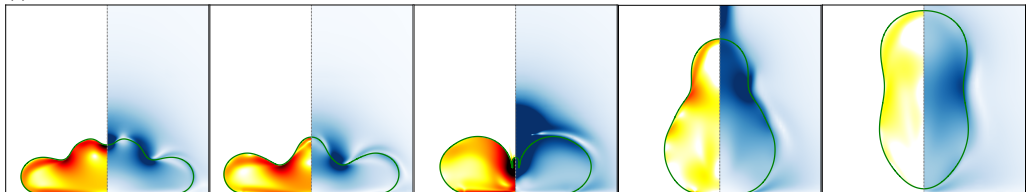
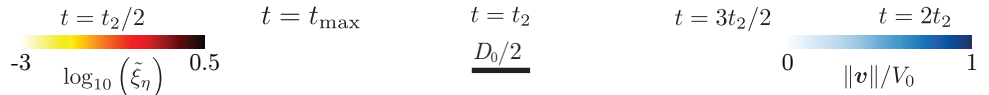
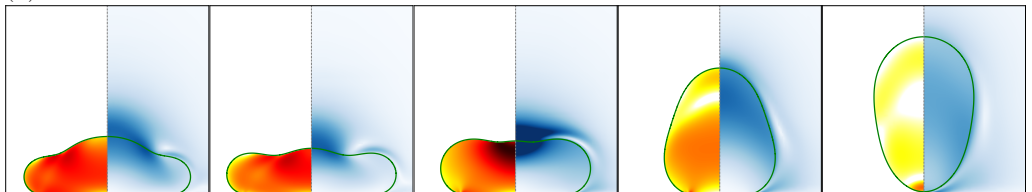
(a) $We = 9, Oh = 0.0025$ (b) $Oh = 0.0025$ (i) $We = 5$ (ii) $We = 12$ (c) $We = 9$ (i) $Oh = 0.005$ (ii) $Oh = 0.05$ 

FIGURE 9. Direct numerical simulations snapshots illustrating the influence of We and Oh on the singular Worthington jet. (a) $(We, Oh) = (9, 0.0025)$, (b) $Oh = 0.0025$ with $We =$ (i) 5 and (ii) 12, and (c) $We = 9$ with $Oh =$ (i) 0.005 and (ii) $Oh = 0.05$. The left-hand side of each numerical snapshot shows the viscous dissipation function ξ_η normalized by inertial scale $\rho_d V_0^3 / D_0$. The right-hand side shows the velocity field magnitude normalized by the impact velocity V_0 .

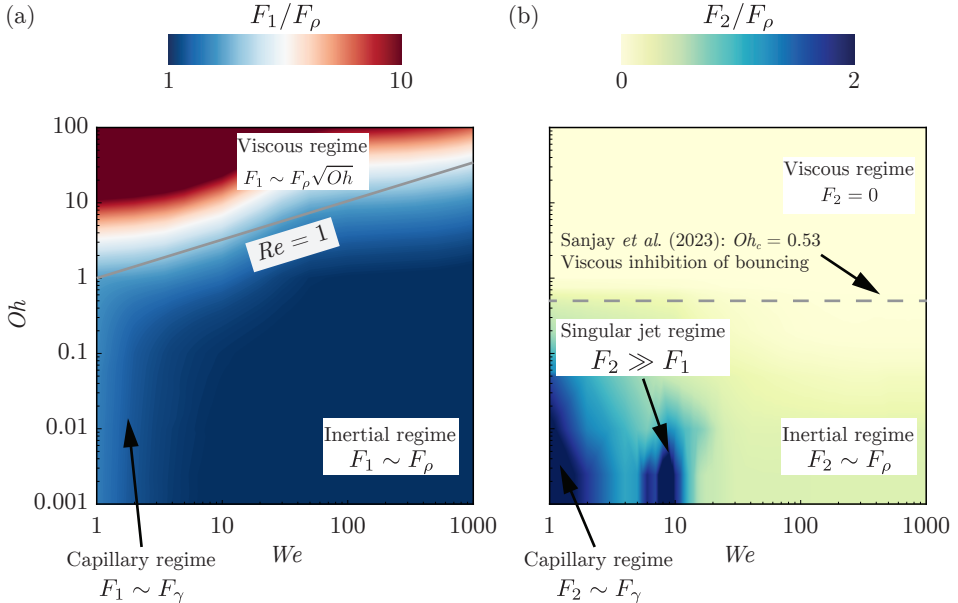


FIGURE 10. Regime map in terms of the drop Ohnesorge number Oh and the impact Weber number We to summarize the two peaks in the impact force by showing the different regimes described in this work based on (a) the first peak in the impact force peak amplitude F_1 and (b) the second peak in the impact force peak amplitude F_2 . Both peaks are normalized by the inertial force scale $F_\rho = \rho_d V_0^2 D_0^2$. These regime maps are constructed using ~ 1500 simulations in the range $0.001 \leq Oh \leq 100$ and $1 \leq We \leq 1000$. The gray solid line in (a) and dashed line in (b) mark the inertial-viscous transition ($Re = 1$) and the bouncing-no-bouncing transition ($Oh_c = 0.53$ for $Bo = 1$, see [Sanjay et al. \(2023a\)](#)), respectively.

Lastly, as Oh increases, bulk dissipation becomes dominant (apparent from increasing Oh at fixed We in figure 8) and can entirely inhibit drop bouncing. Recently, [Jha et al. \(2020\)](#); [Sanjay et al. \(2023a\)](#) showed that there exists a critical Oh , two orders of magnitude higher than that of a 2 mm diameter water drop, beyond which drops do not bounce either, irrespective of their impact velocity. Consequently, the second peak in the impact force diminishes for larger Oh , which explains the monotonic decrease of the amplitude F_2 observed in figure 7 for $We > 30, Oh > 0.01$.

5. Conclusion and outlook

In this work, we study the forces and dissipation encountered during the drop impact process by employing experiments, numerical simulations, and theoretical scaling laws. We vary the two dimensionless control parameters—the Weber (We : dimensionless impact kinetic energy) and the Ohnesorge number (Oh : dimensionless viscosity) independently to elucidate the intricate interplay between inertia, viscosity, and surface tension in governing the forces exerted by a liquid drop upon impact on a non-wetting substrate.

For the first impact force peak amplitude F_1 , owing to the momentum balance after the inertial shock at impact, figure 10(a) summarizes the different regimes in the Oh - We phase space. For low Oh , inertial forces predominantly dictate the impact dynamics, such that F_1 scales with the inertial force F_ρ ([Philippi et al. 2016](#); [Gordillo et al. 2018](#); [Mitchell et al. 2019](#); [Cheng et al. 2022](#); [Zhang et al. 2022](#)) and is insensitive to viscosity variations up to 100-fold. As Oh increases, the viscosity becomes significant, leading to a new scaling law: $F_1 \sim F_\rho \sqrt{Oh}$. The paper unravels this viscous scaling behavior by accounting for

375 the loss of initial kinetic energy owing to viscous dissipation inside the drop. Lastly, at
 376 low We , the capillary pressure inside the drop leads to the scaling $F_1 \sim F_\gamma$ (Moláček &
 377 Bush 2012; Chevy *et al.* 2012).

378 The normal reaction force described in this work is responsible for deforming the
 379 drop as it spreads onto the substrate, where it stops thanks to surface tension. If the
 380 substrate is non-wetting, it retracts to minimize the surface energy and finally takes off
 381 (Richard & Quéré 2000). In this case, the momentum conservation leads to the formation
 382 of a Worthington jet and a second peak in the normal reaction force, as summarized in
 383 figure 10(b). For low Oh and high We , the second force peak amplitude scales with the
 384 inertial force (F_ρ), following a modified Taylor-Culick dynamics (Eggers *et al.* 2010). In
 385 contrast, capillary forces dominate at low We and low Oh , leading to a force amplitude
 386 scaling of $F_2 \sim F_\gamma$. We also identify a narrow regime in the Oh - We phase space where a
 387 singular Worthington jet forms, significantly increasing F_2 (Bartolo *et al.* 2006b; Zhang
 388 *et al.* 2022), localized in the parameter space for $We \approx 9$ and $Oh < 0.01$. As Oh increases,
 389 bulk viscous dissipation counteracts this jet formation, diminishing the second peak and
 390 ultimately inhibiting drop bouncing.

391 Our findings have far-reaching implications, not only enriching the fundamental
 392 understanding of fluid dynamics of drop impact but also informing practical applications
 393 in diverse fields such as inkjet printing, public health, agriculture, and material science
 394 where the entire range of Oh - We phase space is relevant (figures 1b and 10). While this
 395 has identified new scaling laws, it also opens avenues for future research. For instance,
 396 it would be interesting to use the energy accounting approach to unify the scaling laws
 397 for the maximum spreading diameter for arbitrary Oh (Laan *et al.* 2014; Wildeman
 398 *et al.* 2016). Although, the implicit theoretical model summarized in Cheng *et al.* (2022)
 399 describes most of data in figure 5, we stress the importance of having a predictive model
 400 to determine F_1 for given We and Oh (Sanjay & Lohse 2024). The We influence on
 401 the impact force also warrants further exploration, especially in the regime $We \ll 1$ for
 402 arbitrary Oh (Chevy *et al.* 2012; Moláček & Bush 2012) and drop impact on compliant
 403 surfaces (Alventosa *et al.* 2023b; Ma & Huang 2023). Another potential extension of this
 404 work is to non-Newtonian fluids (Martouzet *et al.* 2021; Agüero *et al.* 2022; Bertin 2023;
 405 Jin *et al.* 2023).

406
 407 **Code availability.** The codes used in the present article, [and the parameters and data](#) R2
 408 to reproduce figures 3 and 7 are permanently available at [Sanjay \(2024\)](#).

409
 410 **Acknowledgements.** We would like to thank Vincent Bertin for comments on the
 411 manuscript. We would also like to thank Andrea Prosperetti, Pierre Chantelot, Devaraj
 412 van der Meer, and Uddalok Sen for illuminating discussions.

413
 414 **Funding.** We acknowledge the funding by the ERC Advanced Grant No. 740479-DDD
 415 and NWO-Canon grant FIP-II. B.Z and C.L are grateful for the support from National
 416 Natural Science Foundation of China (Grant No. 12172189, 11921002, 11902179). This
 417 work was carried out on the national e-infrastructure of SURFsara, a subsidiary of SURF
 418 cooperation, the collaborative ICT organization for Dutch education and research. This
 419 work was sponsored by NWO - Domain Science for the use of supercomputer facilities.

420
 421 **Declaration of Interests.** The authors report no conflict of interest.

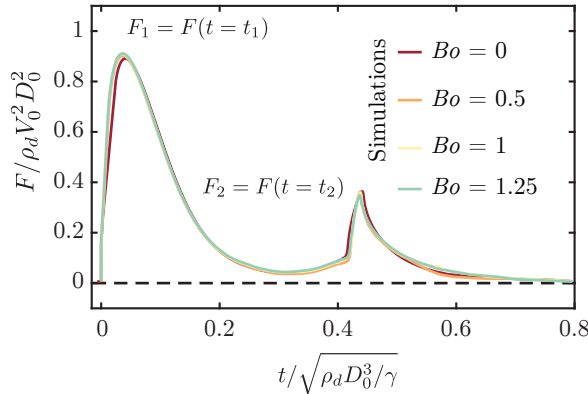


FIGURE A 1. Comparison of the drop impact force $F(t)$ obtained from simulations for the four different Bond numbers $Bo = 0, 0.5, 1, 1.25$. Here, $Oh = 0.06$ and $We = 40$. Both force peaks F_1 and F_2 as well as time to reach these peaks t_1 and t_2 are invariant to variation in Bo .

Author ORCID.

- V. Sanjay <https://orcid.org/0000-0002-4293-6099>;
- B. Zhang <https://orcid.org/0000-0001-8550-2584>;
- C. Lv <https://orcid.org/0000-0001-8016-6462>;
- D. Lohse <https://orcid.org/0000-0003-4138-2255>.

428

Appendix A. Note on the parametric error characterization

R2

This appendix outlines the methodology for characterizing experimental errors in quantification of the drop's size and impact velocities which is crucial for accurate calculation of dimensionless control parameters, We and Oh . The drop diameter determination involves multiple steps. First, we measure the total mass (M_{100}) of 100 drops using an electric balance. From this mass, using the liquid density and assuming spherical shape, we calculated the drop diameter (D_0). We repeated this process five times, yielding $D_{0,1}$ through $D_{0,5}$. The average of these measurements provided the final drop diameter (D_0) and its standard error. For impact velocity determination, we extracted data from experimental high-speed imagery. By tracking the drop center's position in successive frames prior to substrate contact, and knowing the frame rate, we calculated the impact velocity. We repeated this process for five trials, obtaining $V_{0,1}$ through $V_{0,5}$. The average of these values gave the final impact velocity (V_0) and its standard error.

The standard errors for drop diameters do not exceed 0.13 mm. For instance, drops with Ohnesorge numbers of 0.0025, 0.06, and 0.2 have diameters of 2.05 ± 0.13 mm, 2.52 ± 0.11 mm, and 2.54 ± 0.09 mm, respectively. The standard errors for impact velocities did not exceed 0.02 m/s. For the same Oh values, the impact velocities were 1.2 ± 0.002 m/s, 0.97 ± 0.01 m/s, and 0.96 ± 0.01 m/s, respectively. The combined errors in D_0 and V_0 resulted in approximately $\pm 7\%$ error in Weber number We and $\pm 3\%$ error in Ohnesorge number Oh . Consequently, the horizontal error bars, which relate to errors in the control parameters, are smaller than the symbol sizes in our figures.

451

Appendix B. Role of gravity on drop impact forces

R2

Following table 1 and considering the variation in impacting drop diameter (appendix A), the Bond number (equation (1.3)) in our experiments ranges from 0.5 to 1.25,

452

453

454

introducing an additional dimensionless control parameter alongside We and Oh . Gravity typically plays a negligible role in these impact processes (Sanjay *et al.* 2023a; Sanjay & Lohse 2024). We undertook a sensitivity test varying the Bond number from 0 to 1.25 in our simulations. Figure A 1 confirms the leading-order Bond invariance of the results as the impact force profiles, including both force peaks F_1 and F_2 and their corresponding times t_1 and t_2 , remain invariant to these Bond number variations. Notably, while gravity does play a role in drop impact dynamics, particularly for longer time scales and in determining the critical Ohnesorge number Oh_c for bouncing inhibition (see figure 10b and Sanjay *et al.* (2023a)), its effect on the initial impact force peaks is minimal for the parameter range studied here (large Froude numbers, $Fr > 1$). This Bond number invariance allows us to focus on the more dominant effects of Weber and Ohnesorge numbers. Consequently, we selected a representative value of $Bo = 1$, corresponding to a diameter of 0.00254 mm, density 1000 kg/m³, gravitational acceleration 10 m/s², and surface tension 0.061 N/m.

REFERENCES

- AGÜERO, E. A., ALVENTOSA, L. F. L., HARRIS, D. M. & GALEANO-RIOS, C. A. 2022 Impact of a rigid sphere onto an elastic membrane. *Proc. R. Soc. Lond. A* **478** (2266), 20220340.
- AHMAD, M., SCHATZ, M. & CASEY, M. V. 2013 Experimental investigation of droplet size influence on low pressure steam turbine blade erosion. *Wear* **303**, 83–86.
- ALVENTOSA, L. F. L., CIMPEANU, R. & HARRIS, D. M. 2023a Inertio-capillary rebound of a droplet impacting a fluid bath. *J. Fluid Mech.* **958**, A24.
- ALVENTOSA, L. F. L., CIMPEANU, R. & HARRIS, D. M. 2023b Inertio-capillary rebound of a droplet impacting a fluid bath. *J. Fluid Mech.* **958**, A24.
- AMIRZADEH, B., LOUGHALAM, A., RAESSI, M. & TOOTKABONI, M. 2017 A computational framework for the analysis of rain-induced erosion in wind turbine blades. *J. Wind Eng. Ind. Aerodyn.* **163**, 33–43.
- BARTOLO, D., BOUAMRIRENE, F., VERNEUIL, E., BUGUIN, A., SILBERZAN, P. & MOULINET, S. 2006a Bouncing or sticky droplets: Impalement transitions on superhydrophobic micropatterned surfaces. *Europhys. Lett.* **74** (2), 299.
- BARTOLO, D., BOUDAOU, A., NARCY, G. & BONN, D. 2007 Dynamics of non-Newtonian droplets. *Phys. Rev. Lett.* **99** (17), 174502.
- BARTOLO, D., JOSSERAND, C. & BONN, D. 2005 Retraction dynamics of aqueous drops upon impact on non-wetting surfaces. *J. Fluid Mech.* **545**, 329–338.
- BARTOLO, D., JOSSERAND, C. & BONN, D. 2006b Singular jets and bubbles in drop impact. *Phys. Rev. Lett.* **96** (12), 124501.
- BERGERON, V., BONN, D., MARTIN, J. Y. & VOVELLE, L. 2000 Controlling droplet deposition with polymer additives. *Nature* **405** (6788), 772–775.
- BERNY, A., POPINET, S., SÉON, T. & DEIKE, L. 2021 Statistics of jet drop production. *Geophys. Res. Lett.* **48** (10), e2021GL092919.
- BERTIN, V. 2023 Similarity solutions in elastohydrodynamic bouncing. *J. Fluid Mech.* **986**.
- BIANCE, A.-L., CHEVY, F., CLANET, C., LAGUBEAU, G. & QUÉRÉ, D. 2006 On the elasticity of an inertial liquid shock. *J. Fluid Mech.* **554**, 47–66.
- BILOTTO, J., KOLINSKI, J. M., LECAMPION, B., MOLINARI, J.-F., SUBHASH, G. & GARCIA-SUAZER, J. 2023 Fluid-mediated impact of soft solids. *arXiv preprint arXiv:2311.09953*.
- BONN, D., EGGERS, J., INDEKEU, J., MEUNIER, J. & ROLLEY, E. 2009 Wetting and spreading. *Rev. Mod. Phys.* **81** (2), 739–805.
- BORMASHENKO, E., POGREB, R., WHYMAN, G. & ERLICH, M. 2007 Resonance Cassie-Wenzel wetting transition for horizontally vibrated drops deposited on a rough surface. *Langmuir* **23** (24), 12217–12221.
- BOUROUIBA, L. 2021 The fluid dynamics of disease transmission. *Annu. Rev. Fluid Mech.* **53**, 473–508.
- BOUWHUIS, W., VAN DER VEEN, R. C. A., TRAN, T., KEIJ, D. L., WINKELS, K. G., PETERS,

- 507 I. R., VAN DER MEER, D., SUN, C., SNOEIJER, J. H. & LOHSE, D. 2012 Maximal air
508 bubble entrainment at liquid-drop impact. *Phys. Rev. Lett.* **109** (26), 264501.
- 509 BRACKBILL, J. U., KOTHE, D. B. & ZEMACH, C. 1992 A continuum method for modeling
510 surface tension. *J. Comput. Phys.* **100** (2), 335–354.
- 511 CALLIES, M. & QUÉRÉ, D. 2005 On water repellency. *Soft Matter* **1** (1), 55–61.
- 512 CHANTELOT, P. 2018 Rebonds spéciaux de liquides. PhD thesis, Université Paris-Saclay
513 (ComUE).
- 514 CHEN, X., MA, R., LI, J., HAO, C., GUO, W., LUK, B. L., LI, S. C., YAO, S. & WANG, Z.
515 2012 Evaporation of droplets on superhydrophobic surfaces: surface roughness and small
516 droplet size effects. *Phys. Rev. Lett.* **109** (11), 116101.
- 517 CHENG, N.-S. 2008 Formula for the viscosity of a glycerol–water mixture. *Ind. Eng. Chem. Res.*
518 **47** (9), 3285–3288.
- 519 CHENG, X., SUN, T.-P. & GORDILLO, L. 2022 Drop impact dynamics: impact force and stress
520 distributions. *Annu. Rev. Fluid Mech.* **54**, 57–81.
- 521 CHEVY, F., CHEPELIANSKII, A., QUÉRÉ, D. & RAPHAËL, E. 2012 Liquid Hertz contact: softness
522 of weakly deformed drops on non-wetting substrates. *Europhys. Lett.* **100** (5), 54002.
- 523 CHO, H. J., PRESTON, D. J., ZHU, Y. & WANG, E. N. 2016 Nanoengineered materials for
524 liquid–vapour phase-change heat transfer. *Nat. Rev. Mater.* **2** (2), 16092.
- 525 CHUBYNSKY, M. V., BELOUSOV, K. I., LOCKERBY, D. A. & SPRITTLES, J. E. 2020 Bouncing
526 off the walls: the influence of gas-kinetic and van der Waals effects in drop impact. *Phys.*
527 *Rev. Lett.* **124**, 084501.
- 528 CLANET, C., BÉGUIN, C., RICHARD, D. & QUÉRÉ, D. 2004 Maximal deformation of an
529 impacting drop. *J. Fluid Mech.* **517**, 199–208.
- 530 DA VINCI, L. 1508 *Codex Hammer* (earlier *Codex Leicester*). In *The Notebooks of Leonardo da*
531 *Vinci* (ed. and trans. E. MacCurdy).. George Braziller.
- 532 DE GENNES, P. G. 1985 Wetting: statics and dynamics. *Rev. Mod. Phys.* **57**, 827–863.
- 533 DENG, X., MAMMEN, L., BUTT, H.-J. & VOLLMER, D. 2012 Candle soot as a template for a
534 transparent robust superamphiphobic coating. *Science* **335** (6064), 67–70.
- 535 DRISCOLL, M. M. & NAGEL, S. R. 2011 Ultrafast interference imaging of air in splashing
536 dynamics. *Phys. Rev. Lett.* **107** (15), 154502.
- 537 EGGLERS, J., FONTELOS, M. A., JOSSERAND, C. & ZALESKI, S. 2010 Drop dynamics after
538 impact on a solid wall: theory and simulations. *Phys. Fluids* **22** (6), 062101.
- 539 FUKAI, J., SHIIBA, Y., YAMAMOTO, T., MIYATAKE, O., POULIKAKOS, D., MEGARIDIS, C. M.
540 & ZHAO, Z. 1995 Wetting effects on the spreading of a liquid droplet colliding with a flat
541 surface: experiment and modeling. *Phys. Fluids* **7**, 236–247.
- 542 GARCÍA-GEIJO, P., RIBOUX, G. & GORDILLO, JM 2024 The skating of drops impacting over gas
543 or vapour layers. *J. Fluid Mech.* **980**, A35.
- 544 GAUTHIER, A., SYMON, S., CLANET, C. & QUÉRÉ, D. 2015 Water impacting on
545 superhydrophobic macrotextures. *Nat. Commun.* **6** (1), 1–6.
- 546 GOHARDANI, O. 2011 Impact of erosion testing aspects on current and future flight conditions.
547 *Prog. Aerosp. Sci.* **47** (4), 280–303.
- 548 GORDILLO, J. M., RIBOUX, G. & QUINTERO, E. S. 2019 A theory on the spreading of impacting
549 droplets. *J. Fluid Mech.* **866**, 298–315.
- 550 GORDILLO, L., SUN, T.-P. & CHENG, X. 2018 Dynamics of drop impact on solid surfaces:
551 evolution of impact force and self-similar spreading. *J. Fluid Mech.* **840**, 190–214.
- 552 GORIN, B., DI MAURO, G., BONN, D. & KELLAY, H. 2022 Universal aspects of droplet spreading
553 dynamics in Newtonian and non-Newtonian fluids. *Langmuir* **38** (8), 2608–2613.
- 554 HAO, C., LIU, Y., CHEN, X., LI, J., ZHANG, M., ZHAO, Y. & WANG, Z. 2016 Bioinspired
555 interfacial materials with enhanced drop mobility: from fundamentals to multifunctional
556 applications. *Small* **12** (14), 1825–1839.
- 557 HE, L., DING, L., LI, B., MU, W., LI, P. & LIU, F. 2021 Optimization strategy to
558 inhibit droplets rebound on pathogen-modified hydrophobic surfaces. *ACS Appl. Mater.*
559 *Interfaces* **13** (32), 38018–38028.
- 560 HOFFMAN, H., SIJS, R., DE GOEDE, T. & BONN, D. 2021 Controlling droplet deposition with
561 surfactants. *Phys. Rev. Fluids* **6** (3), 033601.
- 562 JHA, A., CHANTELOT, P., CLANET, C. & QUÉRÉ, D. 2020 Viscous bouncing. *Soft Matter* **16**,
563 7270–7273.

- JI, B., YANG, Z. & FENG, J. 2021 Compound jetting from bubble bursting at an air-oil-water interface. *Nat. Commun.* **12** (1), 6305.
- JIN, P., ZHAO, K., BLIN, Z., ALLAIS, M., MOUTERDE, T. & QUÉRÉ, D. 2023 When marbles challenge pearls. *J. Chem. Phys.* **158** (20).
- JOSSERAND, C. & THORODDSEN, S. T. 2016 Drop impact on a solid surface. *Annu. Rev. Fluid Mech.* **48**, 365–391.
- JOWKAR, S. & MORAD, M. R. 2019 Rebounding suppression of droplet impact on hot surfaces: effect of surface temperature and concaveness. *Soft Matter* **15** (5), 1017–1026.
- KIM, J. 2007 Spray cooling heat transfer: The state of the art. *Int. J. Heat Fluid Flow* **28** (4), 753–767.
- KIM, S., WU, Z., ESMALI, E., DOMBROSKIE, J. J & JUNG, S. 2020 How a raindrop gets shattered on biological surfaces. *Proc. Natl. Acad. Sci. U.S.A.* **117** (25), 13901–13907.
- KOLINSKI, J. M., MAHDEVAN, L. & RUBINSTEIN, S. M. 2014 Drops can bounce from perfectly hydrophilic surfaces. *Europhys. Lett.* **108**, 24001.
- KOOIJ, S., SIJS, R., DENN, M. M., VILLERMAUX, E. & BONN, D. 2018 What determines the drop size in sprays? *Phys. Rev. X* **8** (3), 031019.
- LAAN, N., DE BRUIN, K. G., BARTOLO, D., JOSSERAND, C. & BONN, D. 2014 Maximum diameter of impacting liquid droplets. *Phys. Rev. Appl.* **2** (4), 044018.
- LAFUMA, A. & QUÉRÉ, D. 2003 Superhydrophobic states. *Nat. Mater.* **2** (7), 457–460.
- LANGLEY, K., LI, E. Q. & THORODDSEN, S. T. 2017 Impact of ultra-viscous drops: air-film gliding and extreme wetting. *J. Fluid Mech.* **813**, 647–666.
- LESSER, M. B. 1981 Analytic solution of liquid-drop impact problems. *Proc. R. Soc. Lond. A* **377** (1770), 289–308.
- LI, J., ZHANG, B., GUO, P. & LV, Q. 2014 Impact force of a low speed water droplet colliding on a solid surface. *J. Appl. Phys.* **116** (21), 214903.
- LI, Y., QUÉRÉ, D., LV, C. & ZHENG, Q. 2017 Monostable superrepellent materials. *Proc. Natl. Acad. Sci. USA* **114** (13), 3387–3392.
- LIU, M., WANG, S. & JIANG, L. 2017 Nature-inspired superwettability systems. *Nat. Rev. Mater.* **2** (7), 17036.
- LOHSE, D. 2022 Fundamental fluid dynamics challenges in inkjet printing. *Annu. Rev. Fluid Mech.* **54**, 349–382.
- LOHSE, D. & VILLERMAUX, E. 2020 Double threshold behavior for breakup of liquid sheets. *Proc. Natl. Acad. Sci. U.S.A.* **117**, 18912–18914.
- MA, Y. & HUANG, H. 2023 Scaling maximum spreading of droplet impacting on flexible substrates. *J. Fluid Mech.* **958**, A35.
- MANDRE, S., MANI, M. & BRENNER, M. P. 2009 Precursors to splashing of liquid droplets on a solid surface. *Phys. Rev. Lett.* **102** (13), 134502.
- MARTOUZET, G., JØRGENSEN, L., PELET, Y., BIANCE, A.-L. & BARENTIN, C. 2021 Dynamic arrest during the spreading of a yield stress fluid drop. *Phys. Rev. Fluids* **6** (4), 044006.
- MIRELS, H. 1955 Laminar boundary layer behind shock advancing into stationary fluid. *NACA TN* **3401**, 25.
- MITCHELL, B. R., KLEWICKI, J. C., KORKOLIS, Y. P. & KINSEY, B. L. 2019 The transient force profile of low-speed droplet impact: measurements and model. *J. Fluid Mech.* **867**, 300–322.
- MOLÁČEK, J. & BUSH, J. W. M. 2012 A quasi-static model of drop impact. *Phys. Fluids* **24** (12), 127103.
- NEARING, M. A., BRADFORD, J. M. & HOLTZ, R. D. 1986 Measurement of force vs. time relations for waterdrop impact. *Soil Sci. Soc. Am. J.* **50**, 1532–1536.
- PAPADOPOULOS, P., MAMMEN, L., DENG, X., VOLLMER, D. & BUTT, H.-J. 2013 How superhydrophobicity breaks down. *Proc. Natl. Acad. Sci. USA* **110** (9), 3254–3258.
- PHILIPPI, J., LAGRÉE, P.-Y. & ANTOKOWIAK, A. 2016 Drop impact on a solid surface: short-time self-similarity. *J. Fluid Mech.* **795**, 96–135.
- PÖHLKER, M. L., PÖHLKER, C., KRÜGER, O. O., FÖRSTER, J.-D., BERKEMEIER, T., ELBERT, W., FRÖHLICH-NOWOISKY, J., PÖSCHL, U., BAGHERI, G., BODENSCHATZ, E., HUFFMAN, J. A., SCHEITHAUER, S. & MIKHAILOV, E. 2023 Respiratory aerosols and droplets in the transmission of infectious diseases. *Rev. Mod. Phys.* **95** (4), 045001.

- 620 POPINET, S. 2009 An accurate adaptive solver for surface-tension-driven interfacial flows. *J.
621 Comput. Phys.* **228** (16), 5838–5866.
- 622 POPINET, S. 2018 Numerical models of surface tension. *Annu. Rev. Fluid Mech.* **50**, 49–75.
- 623 POPINET, S. & COLLABORATORS 2013–2023 Basilisk C: volume of fluid method. [http://
624 basilisk.fr](http://basilisk.fr) (Last accessed: August 23, 2023).
- 625 QUÉRÉ, D. 2008 Wetting and roughness. *Annu. Rev. Mater. Res.* **38**, 71–99.
- 626 RAMÍREZ-SOTO, O., SANJAY, V., LOHSE, D., PHAM, J. T. & VOLLMER, D. 2020 Lifting a sessile
627 drop from a superamphiphobic surface with an impacting one. *Sci. Adv.* **6**, eaba4330.
- 628 REIN, M. 1993 Phenomena of liquid drop impact on solid and liquid surfaces. *Fluid Dyn. Res.*
629 **12**, 61–93.
- 630 RENARDY, Y., POPINET, S., DUCHEMIN, L., RENARDY, M., ZALESKI, S., JOSSERAND, C.,
631 DRUMRIGHT-CLARKE, M. A., RICHARD, D., CLANET, C. & QUÉRÉ, D. 2003 Pyramidal
632 and toroidal water drops after impact on a solid surface. *J. Fluid Mech.* **484**, 69–83.
- 633 RIBOUX, G. & GORDILLO, J. M. 2014 Experiments of drops impacting a smooth solid surface:
634 a model of the critical impact speed for drop splashing. *Phys. Rev. Lett.* **113** (2), 024507.
- 635 RICHARD, D., CLANET, C. & QUÉRÉ, D. 2002 Contact time of a bouncing drop. *Nature*
636 **417** (6891), 811–811.
- 637 RICHARD, D. & QUÉRÉ, D. 2000 Bouncing water drops. *Europhys. Lett.* **50** (6), 769–775.
- 638 SANJAY, V. 2022 Viscous Free-Surface Flows. PhD thesis, University of Twente.
- 639 SANJAY, V. 2024 Code repository: The role of viscosity on drop impact forces. <https://zenodo.org/doi/10.5281/zenodo.13381995> (Last accessed: Aug 28, 2024).
- 640 SANJAY, V., CHANTELOT, P. & LOHSE, D. 2023a When does an impacting drop stop bouncing?
641 *Journal of Fluid Mechanics* **958**, A26.
- 642 SANJAY, V., LAKSHMAN, S., CHANTELOT, P., SNOEIJER, J. H. & LOHSE, D. 2023b Drop impact
643 on viscous liquid films. *J. Fluid Mech.* **958**, A25.
- 644 SANJAY, V. & LOHSE, D. 2024 Unifying theory of scaling in drop impact: Forces & maximum
645 spreading diameter. *arXiv preprint arXiv: 2408.12714*.
- 646 SANJAY, V., LOHSE, D. & JALAAL, M. 2021 Bursting bubble in a viscoplastic medium. *J. Fluid
647 Mech.* **922**, A2.
- 648 SANJAY, V., SEN, U., KANT, P. & LOHSE, D. 2022 Taylor-Culick retractions and the influence
649 of the surroundings. *J. Fluid Mech.* **948**, A14.
- 650 SBRAGAGLIA, M., PETERS, A. M., PIRAT, C., BORKENT, B. M., LAMMERTINK, R. G. H.,
651 WESSLING, M. & LOHSE, D. 2007 Spontaneous breakdown of superhydrophobicity. *Phys.
652 Rev. Lett.* **99** (15), 156001.
- 653 SCHLICHTING, H. 1968 *Boundary-layer theory*. McGraw-Hill.
- 654 SCHROLL, R. D., JOSSERAND, C., ZALESKI, S. & ZHANG, W. W. 2010 Impact of a viscous
655 liquid drop. *Phys. Rev. Lett.* **104** (3), 034504.
- 656 SHARMA, P. K. & DIXIT, H. N. 2021 Regimes of wettability-dependent and wettability-
657 independent bouncing of a drop on a solid surface. *J. Fluid Mech.* **908**, A37.
- 658 SHIRI, S. & BIRD, J. C. 2017 Heat exchange between a bouncing drop and a superhydrophobic
659 substrate. *Proc. Natl. Acad. Sci. U.S.A.* **114** (27), 6930–6935.
- 660 SIJS, R. & BONN, D. 2020 The effect of adjuvants on spray droplet size from hydraulic nozzles.
661 *Pest. Manage. Sci.* **76** (10), 3487–3494.
- 662 SMITH, F. R. & BRUTIN, D. 2018 Wetting and spreading of human blood: recent advances and
663 applications. *Curr. Opin. Colloid Interface Sci.* **36**, 78–83.
- 664 SMITH, F. R., NICLOUX, C. & BRUTIN, D. 2018 Influence of the impact energy on the pattern
665 of blood drip stains. *Phys. Rev. Fluids* **3** (1), 013601.
- 666 SMITH, M. I. & BERTOLA, V. 2010 Effect of polymer additives on the wetting of impacting
667 droplets. *Phys. Rev. Lett.* **104**, 154502.
- 668 SOTO, D., DE LARIVIERE, A. B., BOUTILLON, X., CLANET, C. & QUÉRÉ, D. 2014 The force
669 of impacting rain. *Soft Matter* **10** (27), 4929–4934.
- 670 SPRITTLES, JAMES E 2024 Gas microfilms in droplet dynamics: When do drops bounce? *Annu.
671 Rev. Fluid Mech.* **56**, 91–118.
- 672 THORAVAL, M.-J., SCHUBERT, J., KARPITSCHKA, S., CHANANA, M., BOYER, F., SANDOVAL-
673 NAVAL, E., DIJKSMAN, J. F., SNOEIJER, J. H. & LOHSE, D. 2021 Nanoscopic interactions
674 of colloidal particles can suppress millimetre drop splashing. *Soft Matter* **17** (20), 5116–
675 5121.

- 677 THORAVAL, M.-J., TAKEHARA, K., ETOH, T. G. & THORODDSEN, S. T. 2013 Drop impact
678 entrapment of bubble rings. *J. Fluid Mech.* **724**, 234–258.
- 679 TSAI, P., LAMMERTINK, R. G. H., WESSLING, M. & LOHSE, D. 2010 Evaporation-triggered
680 wetting transition for water droplets upon hydrophobic microstructures. *Phys. Rev. Lett.*
681 **104** (11), 116102.
- 682 TUTEJA, A., CHOI, W., MA, M., MABRY, J. M., MAZZELLA, S. A., RUTLEDGE, G. C.,
683 MCKINLEY, G. H. & COHEN, R. E. 2007 Designing superoleophobic surfaces. *Science*
684 **318** (5856), 1618–1622.
- 685 VILLERMAUX, E. 2020 Fragmentation versus cohesion. *J. Fluid Mech.* **898**, P1.
- 686 VILLERMAUX, E. & BOSSA, B. 2011 Drop fragmentation on impact. *J. Fluid Mech.* **668**, 412–
687 435.
- 688 VILLERMAUX, E., WANG, X. & DEIKE, L. 2022 Bubbles spray aerosols: certitudes and mysteries.
689 *Proc. Natl. Acad. Sci. Nexus* **1** (5), pgac261.
- 690 VOLK, A. & KÄHLER, C. J. 2018 Density model for aqueous glycerol solutions. *Exp. Fluids*
691 **59** (5), 75.
- 692 WAGNER, H. 1932 Über Stoß- und Gleitvorgänge an der Oberfläche von Flüssigkeiten. *Z. Angew.*
693 *Math. Mech.* **12** (4), 193–215.
- 694 WILDEMAN, S., VISSER, C. W., SUN, C. & LOHSE, D. 2016 On the spreading of impacting
695 drops. *J. Fluid Mech.* **805**, 636–655.
- 696 WORTHINGTON, A. M. 1876a On the forms assumed by drops of liquids falling vertically on a
697 horizontal plate. *Proc. R. Soc.* **25** (171–178), 261–272.
- 698 WORTHINGTON, A. M. 1876b A second paper on the forms assumed by drops of liquids falling
699 vertically on a horizontal plate. *Proc. R. Soc.* **25** (171–178), 498–503.
- 700 WU, S., DU, Y., ALSAID, Y., WU, D., HUA, M., YAN, Y., YAO, B., MA, Y., ZHU, X. & HE,
701 X. 2020 Superhydrophobic photothermal icephobic surfaces based on candle soot. *Proc.*
702 *Natl Acad. Sci. USA* **117** (21), 11240–11246.
- 703 XU, L., ZHANG, W. W. & NAGEL, S. R. 2005 Drop splashing on a dry smooth surface. *Phys.*
704 *Rev. Lett.* **94** (18), 184505.
- 705 YARIN, A. L. 2006 Drop impact dynamics: splashing, spreading, receding, bouncing... *Annu.*
706 *Rev. Fluid Mech.* **38**, 159–192.
- 707 YARIN, A. L., ROISMAN, I. V. & TROPEA, C. 2017 *Collision Phenomena in Liquids and Solids*.
708 Cambridge University Press.
- 709 YUN, S. 2017 Bouncing of an ellipsoidal drop on a superhydrophobic surface. *Sci. Rep.* **7** (1),
710 17699.
- 711 ZHANG, B., LI, J., GUO, P. & LV, Q. 2017 Experimental studies on the effect of reynolds and
712 weber numbers on the impact forces of low-speed droplets colliding with a solid surface.
713 *Exp. Fluids* **58** (9), 1–12.
- 714 ZHANG, B., SANJAY, V., SHI, S., ZHAO, Y., LV, C. & LOHSE, D. 2022 Impact forces of water
715 drops falling on superhydrophobic surfaces. *Phys. Rev. Lett.* **129**, 104501.
- 716 ZHANG, R., ZHANG, B., LV, Q., LI, J. & GUO, P. 2019 Effects of droplet shape on impact
717 force of low-speed droplets colliding with solid surface. *Exp. Fluids* **60** (4), 64.
- 718 ZHENG, S., DILLAVOU, S. & KOLINSKI, J. M. 2021 Air mediates the impact of a compliant
719 hemisphere on a rigid smooth surface. *Soft Matter* **17** (14), 3813–3819.